

# Ringdown of a black hole embedded in a Burkert dark matter halo

Yi Yang,<sup>1,\*</sup> Gaetano Lambiase ,<sup>2,3,†</sup> Ali Övgün ,<sup>4,‡</sup> Dong Liu,<sup>5,§</sup> and Zheng-Wen Long<sup>5,¶</sup>

<sup>1</sup>*School of Mathematics and Statistics,*

*Guizhou University of Finance and Economics, Guiyang, 550025, China*

<sup>2</sup>*Dipartimento di Fisica “E.R Caianiello”, Universit degli Studi di Salerno,  
Via Giovanni Paolo II, 132 - 84084 Fisciano (SA), Italy*

<sup>3</sup>*Istituto Nazionale di Fisica Nucleare - Gruppo Collegato di Salerno - Sezione di Napoli,  
Via Giovanni Paolo II, 132 - 84084 Fisciano (SA), Italy*

<sup>4</sup>*Physics Department, Eastern Mediterranean University,  
Famagusta, 99628 North Cyprus via Mersin 10, Turkey*

<sup>5</sup>*College of Physics, Guizhou University, Guiyang, 550025, China*

We construct a new static, spherically symmetric black hole spacetime embedded in a dark matter halo whose density follows the cored Burkert profile. Starting from the halo-only geometry determined by the rotation-curve relation, we solve the Einstein equations with the Burkert stress-energy and enforce a Schwarzschild boundary condition, obtaining closed-form metric functions in which the halo contribution deforms the redshift/shape functions and reduces to the Schwarzschild limit when the halo parameters vanish. On this background we study linear perturbations of test fields with spins  $s = 0, 1, 2$  and compute their quasinormal spectra using both a high-order WKB scheme and Leaver’s continued-fraction method, complemented by time-domain evolutions. We find that increasing either the Burkert core radius  $r_0$  or the central density  $\rho_0$  generically shifts the real part of the frequencies upward and enhances damping, while the multipole index  $l$  primarily increases the oscillation frequency with a milder impact on the decay rate. The two frequency-extraction methods agree to within small, systematic offsets across the explored parameter space. Our results quantify how a cored dark matter environment imprints itself on the ringdown of a central black hole and provide benchmarks for future gravitational-wave tests of halo properties.

Keywords: Black holes; Dark matter; Quasinormal modes

## I. INTRODUCTION

Accounting for approximately 25% of the universe’s total energy density, dark matter (DM) is a critical component that governs the formation and dynamics of structures, ranging from galaxies to clusters.[1]. Its presence is inferred from multiple, complementary probes including galaxy rotation curves, strong/weak lensing maps, satellite kinematics, and the cosmic microwave background-which collectively require mass distributions exceeding that of baryons [2–4]. On galactic radii, the inner shape of the DM density remains under active debate: cold DM simulations typically predict cuspy inner profiles (e.g., Navarro–Frenk–White (NFW)), whereas observations of low-surface-brightness and dwarf galaxies often favor cored profiles with nearly constant central density; the Burkert parameterization has proven particularly successful at fitting both inner kinematics and outer rotation-curve declines [3, 5–7]. In this work we focus on how such cored halos backreact on black hole (BH) spacetimes and how gravitational observables may, in turn, constrain halo properties.

BHs embedded in galactic DM halos offer a controlled setting to investigate how non-baryonic matter backreacts on strong-gravity spacetimes and, in turn, how gravity can be used to probe the microphysics of the halo. In the concordance cosmology, DM governs the assembly of structure from sub-galactic to cluster scales [1]. On galactic radii, multiple and complementary observations-including rotation curves, strong and weak lensing, and dynamical inferences-require extended mass components in excess of luminous matter [2, 3]. An Einstein-cluster of orbiting collisionless particles was shown to naturally yield a central, spiky DM distribution that can impact galactic centers and their relativistic phenomenology [8]. A vector-field action was proposed that reproduces the Einstein-cluster phenomenology for DM, establishing a principled relativistic framework and discussing equilibrium and stability [9]. The appearance (e.g., shadow/lensing) and gravitational-wave emission of BHs were quantified for generic DM profiles, demonstrating profile-dependent shifts in images and ringdown spectra [10]. A BH spacetime embedded in a Dekel–Zhao DM halo was constructed and its observable signatures-including geodesics, lensing, and quasinormal modes-were analyzed [11]. Event Horizon Telescope constraints were translated into bounds on BH solutions with

\*Electronic address: [yiyang@mail.gufe.edu.cn](mailto:yiyang@mail.gufe.edu.cn)

†Electronic address: [lambiase@sa.infn.it](mailto:lambiase@sa.infn.it)

‡Electronic address: [ali.ovgun@emu.edu.tr](mailto:ali.ovgun@emu.edu.tr)

§Electronic address: [dongliuvv@yeah.net](mailto:dongliuvv@yeah.net)

¶Electronic address: [zwlong@gzu.edu.cn](mailto:zwlong@gzu.edu.cn)

DM in the presence of a generalized-uncertainty-principle minimal length [12]. A static BH solution surrounded by a pseudo-isothermal halo was derived and its perturbative and observational imprints were explored [13]. BH phenomenology in quantum (wave/fuzzy) DM was investigated, highlighting distinctive lensing and dynamical effects relative to standard halos [14]. Gravitational ringing and superradiant instabilities of Kerr-like BHs were studied within a DM halo, revealing modifications to spectra and potential instability windows [15]. The weak deflection angle produced by BHs at the centers of the Milky Way and M87 was shown to receive measurable corrections from surrounding DM density profiles such as the cold DM, scalar field DM, and the universal rotation curve [16]. DM support for traversable wormhole configurations was examined in the ultra-diffuse galaxy Dragonfly 44, illustrating conditions for wormhole formation within galactic environments [17].

From a phenomenological standpoint, the radial DM distribution is often modeled by either cuspy or cored profiles. While cold-DM simulations generically favor centrally rising (NFW-like) cusps [5], a wide class of low-surface-brightness and dwarf galaxies is better described by cored profiles with approximately constant central density. A widely used cored parameterization is the *Burkert* profile [18]

$$\rho_{\text{Bur}}(r) = \frac{\rho_0}{(1 + r/r_0)[1 + (r/r_0)^2]}, \quad (1)$$

which simultaneously fits inner kinematics and the outer decline of rotation curves [6, 7]. The pair  $(\rho_0, r_0)$  encapsulates the core density and scale radius and empirically exhibits tight scaling relations across galaxy samples [3].

Embedding a BH in such an environment raises two interrelated questions. First, how does the halo stress–energy modify the redshift and shape functions of the background geometry in a spherically symmetric, stationary configuration? Second, how do these modifications imprint on observables tied to null and timelike geodesics—e.g., quasinormal-mode (QNM) spectra, time-domain ringdown, and potentially lensing and shadow features? A pragmatic route, which we follow here, is to start from a halo-only spacetime whose redshift function is fixed by the measured circular velocity, and then solve the Einstein equations with the DM stress–energy while enforcing a Schwarzschild boundary condition for the central object [19, 20]. This construction yields an analytic metric that (i) reduces continuously to Schwarzschild in the vanishing-halo limit, and (ii) makes explicit how  $(\rho_0, r_0)$  renormalize the effective potential felt by perturbations.

Gravitational perturbations of BH spacetimes are encoded in discrete, complex QNM frequencies that control the late-time ringdown [21, 22]. The real part sets the oscillation frequency and the imaginary part the damping time; both are exquisitely sensitive to the near-horizon geometry and to any environmental matter distributions encountered by radiation or perturbations on their way out [23]. QNMs thus provide a clean target for current and next-generation gravitational-wave (GW) detectors to test strong-field gravity and to search for beyond-vacuum imprints [24]. In matter-surrounded or “dirty” BHs, even modest departures from vacuum can generate systematic, profile-dependent shifts in the spectrum [21, 22].

In this work we construct a static, spherically symmetric BH surrounded by a Burkert halo and analyze its linear response to scalar, electromagnetic, and gravitational perturbations. We compute QNMs using Leaver’s continued-fraction method alongside high-order WKB estimates and validate trends with time-domain evolutions. We find that increasing either the core radius  $r_0$  or the central density  $\rho_0$  enhances the real part of the frequency and the magnitude of the damping rate across spins  $s = 0, 1, 2$ , while the multipole index primarily controls the oscillation frequency. These results deliver quantitative benchmarks for ringdown-based constraints on cored halos and motivate extensions to rotating BHs and to broader classes of cored and cuspy profiles.

## II. SPHERICALLY SYMMETRIC BH METRIC SURROUNDED BY THE BURKERT PROFILE

In this work, we study the Burkert profile, which is a model describing the density distribution of DM in galaxies, particularly low surface brightness and dwarf galaxies. Using Burkert profile DM density given in (1), we derive a spherically symmetric BH solution surrounded by DM. To do so, it is essential to first determine the mass distribution of the DM halo. Using the above DM halo profile, the corresponding mass profile can be calculated [25]

$$\begin{aligned} M_{\text{Bur}} &= 4\pi \int_0^r \rho_{\text{Bur}}(r') r'^2 dr' \\ &= \pi \rho_0 r_0^3 \left( \ln(r_0^2 + r^2) + 2 \ln(r_0 + r) - 2 \tan^{-1}\left(\frac{r}{r_0}\right) - 4 \ln r_0 \right). \end{aligned} \quad (2)$$

In a spherically symmetric spacetime, the tangential velocity of a test particle within the DM halo can be derived based on the halo’s mass distribution. As a result, the tangential velocity (using units  $G = 1, c = 1$ ) is obtained

$$V_{\text{Bur}} = \sqrt{\frac{M_{\text{Bur}}}{r}} = \sqrt{\frac{\pi \rho_0 r_0^3 \left( \ln(r_0^2 + r^2) + 2 \ln(r_0 + r) - 2 \tan^{-1}\left(\frac{r}{r_0}\right) - 4 \ln r_0 \right)}{r}}. \quad (3)$$

The line element for a spherically symmetric spacetime representing a pure DM halo can be expressed (using the approach outlined in Ref. [25] and subsequently applied by Xu et al. in Ref. [26])

$$ds^2 = -\mathcal{N}(r)dt^2 + \mathcal{G}(r)^{-1}dr^2 + r^2(d\theta^2 + \sin^2\theta d\phi^2), \quad (4)$$

where the  $\mathcal{N}(r)$  denotes the redshift functions, and  $\mathcal{G}(r)$  represents the shape functions. The tangential velocity is intrinsically associated with the redshift function  $\mathcal{N}(r)$  in the spacetime metric, which is given by

$$V_{Bur}^2 = r \frac{d \ln \sqrt{\mathcal{N}(r)}}{dr}. \quad (5)$$

It is important to emphasize that, in our study, we focus on the scenario where  $\mathcal{N}(r) = \mathcal{G}(r)$ . By substituting equation (3) into the previous equation, we are able to derive the analytical expressions for the redshift and shape functions in the background of a pure DM metric

$$\begin{aligned} \mathcal{N}_{Bur}(r) &= \mathcal{G}_{Bur}(r) \\ &= r_0^{\frac{8\pi\rho_0 r_0^3}{r}} (r_0 + r)^{-\frac{4\pi\rho_0 r_0^3}{r} - 4\pi\rho_0 r_0^2} (r_0^2 + r^2)^{2\pi\rho_0 r_0^2 - \frac{2\pi\rho_0 r_0^3}{r}} e^{\frac{4\pi\rho_0 r_0^2(r_0 + r) \arctan(\frac{r}{r_0})}{r}}. \end{aligned} \quad (6)$$

We will now solve the Einstein field equations to derive the spherically symmetric BH metric surrounded by a Burkert profile halo. According to the method suggested by Xu et al. [26], it is necessary to solve the Einstein field equation for a spacetime dominated by the pure Burkert profile DM, which can be expressed as

$$R_{\mu\nu} - \frac{1}{2}g_{\mu\nu}R = \kappa^2 T_{\mu\nu}(\text{BUR}), \quad (7)$$

where  $g_{\mu\nu}$  represents the metric tensor of the pure Burkert profile DM spacetime.  $R_{\mu\nu}$  and  $R$  is the Ricci tensor and Ricci scalar, respectively. The energy-momentum tensor for the pure Burkert profile DM spacetime is expressed as  $T^\nu{}_\mu = g^{\nu\sigma}T_{\mu\sigma} = \text{diag}[-\rho, p_r, p, p]$ . From this, we can derive the necessary equations

$$\begin{aligned} \kappa^2 T^t{}_t(\text{BUR}) &= \mathcal{G}_{Bur}(r) \left( \frac{1}{r} \frac{\mathcal{G}'_{Bur}(r)}{\mathcal{G}_{Bur}(r)} + \frac{1}{r^2} \right) - \frac{1}{r^2}, \\ \kappa^2 T^r{}_r(\text{BUR}) &= \mathcal{G}_{Bur}(r) \left( \frac{1}{r^2} + \frac{1}{r} \frac{\mathcal{N}'_{Bur}(r)}{\mathcal{N}_{Bur}(r)} \right) - \frac{1}{r^2}, \\ \kappa^2 T^\theta{}_\theta(\text{BUR}) &= \kappa^2 T^\phi{}_\phi(\text{BUR}) = \frac{1}{2} \mathcal{G}_{Bur}(r) \times \\ &\left[ \frac{\mathcal{N}''_{Bur}(r)\mathcal{N}_{Bur}(r) - \mathcal{N}'^2_{Bur}(r)}{\mathcal{N}^2_{Bur}(r)} + \frac{\mathcal{N}'^2_{Bur}(r)}{2\mathcal{N}^2_{Bur}(r)} \right. \\ &\left. + \frac{1}{r} \left( \frac{\mathcal{N}'_{Bur}(r)}{\mathcal{N}_{Bur}(r)} + \frac{\mathcal{G}'_{Bur}(r)}{\mathcal{G}_{Bur}(r)} \right) + \frac{\mathcal{N}'_{Bur}(r)\mathcal{G}'_{Bur}(r)}{2\mathcal{N}_{Bur}(r)\mathcal{G}_{Bur}(r)} \right]. \end{aligned} \quad (8)$$

We consider a BH surrounded by the Burkert profile DM halo, therefore the total energy-momentum tensor is given by  $T^\nu{}_\mu = T^\nu{}_\mu(\text{BH}) + T^\nu{}_\mu(\text{BUR})$ . According to General Relativity, the Schwarzschild BH is a vacuum solution, meaning it satisfies the condition  $T^\nu{}_\mu(\text{BH}) = 0$ . When considering a Schwarzschild-like BH surrounded by the Burkert profile halo, we only need to take into account the energy-momentum tensor of the DM halo. Hence, we assume that the BH metric, encircled by the Burkert profile DM, takes the following structure

$$ds^2 = -[\mathcal{N}_{Bur}(r) + X_1(r)]dt^2 + \frac{1}{\mathcal{G}_{Bur}(r) + X_2(r)}dr^2 + r^2(d\theta^2 + \sin^2\theta d\phi^2), \quad (9)$$

where the specific expression of  $\mathcal{N}_{Bur}(r)$  and  $\mathcal{G}_{Bur}(r)$  is shown in Eq. (6). The functions  $X_1(r)$  and  $X_2(r)$  are determined by the parameters of BH and the Burkert profile DM parameters. Consequently, the Einstein field equations can be reformulated as

$$R_{\mu\nu} - \frac{1}{2}g_{\mu\nu}R = \kappa^2 [T_{\mu\nu}(\text{BH}) + T_{\mu\nu}(\text{BUR})]. \quad (10)$$

By inserting the modified BH metric (9) into the Einstein field equations mentioned above, we derive

$$[\mathcal{G}_{Bur}(r) + X_2(r)] \left[ \frac{1}{r^2} + \frac{1}{r} \frac{\mathcal{G}'_{Bur}(r) + X'_2(r)}{\mathcal{G}_{Bur}(r) + X_2(r)} \right] = \mathcal{G}_{Bur}(r) \left[ \frac{1}{r^2} + \frac{1}{r} \frac{\mathcal{G}'_{Bur}(r)}{\mathcal{G}_{Bur}(r)} \right], \quad (11a)$$

$$[\mathcal{G}_{Bur}(r) + X_2(r)] \left[ \frac{1}{r^2} + \frac{1}{r} \frac{\mathcal{N}'_{Bur}(r) + X'_1(r)}{\mathcal{N}_{Bur}(r) + X_1(r)} \right] = \mathcal{G}_{Bur}(r) \left[ \frac{1}{r^2} + \frac{1}{r} \frac{\mathcal{N}'_{Bur}(r)}{\mathcal{N}_{Bur}(r)} \right]. \quad (11b)$$

By considering the Schwarzschild BH as the boundary condition for the system, the analytical solution to the two differential equations can be determined (in units G=1)

$$\begin{aligned} X_2(r) &= -\frac{2M}{r}, \\ X_1(r) &= \exp \left\{ \int \frac{\mathcal{G}_{Bur}(r)}{\mathcal{G}_{Bur}(r) + X_2(r)} \left[ \frac{1}{r} + \frac{\mathcal{N}'_{Bur}(r)}{\mathcal{N}_{Bur}(r)} \right] dr - \frac{1}{r} dr \right\} - \mathcal{N}_{Bur}(r). \end{aligned} \quad (12)$$

For the Burkert profile, when  $\mathcal{N}_{Bur}(r) = \mathcal{G}_{Bur}(r)$ , we find that  $X_1(r) = X_2(r) = -2M/r$ . Therefore, the BH solution in the presence of the Burkert profile DM halo can be expressed as follows

$$ds^2 = -F_1(r)dt^2 + \frac{1}{F_2(r)}dr^2 + \mathcal{R}(r)(d\theta^2 + \sin^2\theta d\phi^2), \quad (13)$$

where  $\mathcal{R}(r) = r^2$ , and  $F_1 = X_1(r) + \mathcal{N}_{Bur}(r) = F_2 = X_2(r) + \mathcal{G}_{Bur}(r)$ , whose explicit expressions are

$$F_1(r) = F_2(r) = r_0^{\frac{8\pi\rho_0r_0^3}{r}}(r_0+r)^{-\frac{4\pi\rho_0r_0^3}{r}-4\pi\rho_0r_0^2} \times (r_0^2+r^2)^{2\pi\rho_0r_0^2-\frac{2\pi\rho_0r_0^3}{r}} e^{\frac{4\pi\rho_0r_0^2(r_0+r)\arctan(\frac{r}{r_0})}{r}} - \frac{2M}{r}. \quad (14)$$

### III. LINEAR PERTURBATIONS: UNIFIED MASTER EQUATION FOR $s = 0, 1, 2$

Below we summarize the effective potentials  $V(r)$  in a compact “metric–first” form that depends only on  $F(r)$  and its derivatives.

#### A. Scalar perturbation of the BH (generic $F(r)$ )

We begin with a minimally coupled, massless scalar test field on the background

$$ds^2 = -F(r)dt^2 + \frac{dr^2}{F(r)} + r^2d\Omega^2, \quad \frac{dr_*}{dr} = \frac{1}{F(r)}, \quad (15)$$

where  $r_*$  is the tortoise coordinate. Using the separation ansatz  $\Psi(t, r, \theta, \phi) = \frac{u_l(r)}{r} Y_{lm}(\theta, \phi) e^{-i\omega t}$ , the Klein–Gordon equation  $\square\Psi = 0$  reduces to the Schrödinger-like master equation

$$\frac{d^2u_l}{dr_*^2} + [\omega^2 - V_0(r)]u_l = 0, \quad V_0(r) = F(r) \left[ \frac{l(l+1)}{r^2} + \frac{F'(r)}{r} \right]. \quad (16)$$

Thus, for scalar perturbations the halo affects the barrier only through  $F$  and its first derivative. Quasinormal modes (QNMs) satisfy purely ingoing (outgoing) boundary conditions at the event horizon (spatial infinity) in the  $r_*$  coordinate.

#### B. Electromagnetic perturbation (generic $F(r)$ )

Maxwell perturbations on static, spherically symmetric backgrounds with  $g_{tt}g_{rr} = -1$  split into axial/polar sectors that are isospectral. After expanding  $A_\mu$  in vector spherical harmonics and eliminating gauge redundancies, one obtains the same master form,

$$\frac{d^2u_l}{dr_*^2} + [\omega^2 - V_1(r)]u_l = 0, \quad V_1(r) = F(r) \frac{l(l+1)}{r^2}, \quad l \geq 1. \quad (17)$$

Compared to the scalar case, the  $F'(r)$  term is absent; the background enters only through the overall factor  $F(r)$ .

#### C. Axial gravitational perturbation (generic $F(r)$ )

For axial (odd-parity) metric perturbations in the Regge–Wheeler gauge [22], the single gauge-invariant master variable obeys

$$\frac{d^2u_l}{dr_*^2} + [\omega^2 - V_2(r)]u_l = 0, \quad V_2(r) = F(r) \left[ \frac{l(l+1)}{r^2} - \frac{3F'(r)}{r} \right], \quad l \geq 2. \quad (18)$$

Equation (18) reproduces the standard Regge–Wheeler potential in the vacuum limit  $F(r) = 1 - 2M/r$  and continuously incorporates the deformation due to halo through  $F$  and  $F'$ .<sup>1</sup>

In our model  $F(r) = F_1(r) = F_2(r) = \mathcal{N}_{Bur}(r) - 2M/r$ , with  $\mathcal{N}_{Bur}(r)$  given by Eq. (6). Substituting this  $F(r)$  into Eqs. (16)–(18) yields the explicit scalar, electromagnetic, and axial-gravitational effective potentials used in Sec. IV for the WKB, continued-fraction, and time-domain analyses.

#### IV. THE QNM OF THE BH SURROUNDED BY THE BURKERT PROFILE

##### A. Leaver's continued fraction method

In this part, we introduce the continued fraction approach for computing quasinormal modes (QNMs). Among the available techniques, it is considered one of the most accurate and effective. Originally proposed by Leaver [27, 28] in the context of Kerr BHs, this method has since evolved into a standard tool for analyzing BH perturbations and extracting their QNM spectra, owing to its robustness and high precision. To implement the procedure, one begins with the radial equation, imposing the appropriate boundary conditions at spatial infinity and near the event horizon, which yield the corresponding asymptotic forms of the solutions, who applied it to study the QNMs of Kerr BHs. Subsequently, it has become a foundational tool in the study of BH perturbations and their associated QNMs due to its precision and reliability.

In addition, considering that no radiation can escape from a BH, the boundary conditions are specified as a purely outgoing wave ( $e^{i\omega r}$ ) at spatial infinity and a purely ingoing wave ( $-e^{i\omega r}$ ) at the event horizon. Therefore, one can obtain the asymptotic solutions

$$R(r) \approx \begin{cases} e^{i\omega r} r^{i\omega r_h}, & r \rightarrow \infty, \\ e^{-i\omega r_h} (r - r_h)^{-i\omega r_h}, & r \rightarrow r_h. \end{cases} \quad (19)$$

In view of this, we search for a solution of the form

$$R(r) = e^{i\omega r} r^{i\omega r_h} \left( \frac{r - r_h}{r} \right)^{-i\omega r_h} \sum_{n=0}^{\infty} a_n \left( \frac{r - r_h}{r} \right)^n. \quad (20)$$

Using this form of the solution, the following recurrence relation can be derived

$$\alpha_0 a_1 + \beta_0 a_0 = 0 \quad (21)$$

and

$$\alpha_n a_{n+1} + \beta_n a_n + \gamma_n a_{n-1} = 0, \quad n \geq 1, \quad (22)$$

where the recurrence relation coefficients can be written as

$$\begin{aligned} \alpha_n &= 2M(n+1) \left( 2\pi^2 \rho_0 r_0^2 + 1 \right) \left( -4M\omega \sqrt{-(2\pi^2 \rho_0 r_0^2 + 1)^2} \right. \\ &\quad \left. + 4\pi^4 (n+1) \rho_0^2 r_0^4 + 4\pi^2 (n+1) \rho_0 r_0^2 + n+1 \right), \end{aligned} \quad (23)$$

$$\begin{aligned} \beta_n &= -2M \left( l^2 + l + 2n(n+1) + 1 \right) \left( 2\pi^2 \rho_0 r_0^2 + 1 \right)^3 \\ &\quad + 32M^3 \omega^2 \left( 2\pi^2 \rho_0 r_0^2 - i\sqrt{-(2\pi^2 \rho_0 r_0^2 + 1)^2} + 1 \right) + 8M^2 (2n+1) \omega \\ &\quad \times \left( 2i\pi^2 \rho_0 r_0^2 + \sqrt{-(2\pi^2 \rho_0 r_0^2 + 1)^2} + i \right) (2\pi^2 \rho_0 r_0^2 + 1) + s^2 (2\pi^2 \rho_0 r_0^2 + 1)^4, \end{aligned} \quad (24)$$

---

<sup>1</sup> In matter-supported geometries, even-parity (polar) perturbations can couple to stress–energy perturbations and lead to a modified Zerilli potential. Since our QNM analysis targets the leading geometry-driven effects, we focus on the axial sector; the polar sector follows analogously once a matter perturbation prescription is fixed.

$$\begin{aligned}
\gamma_n = & 16iM^3\omega^2 \left( 2i\pi^2\rho_0r_0^2 + \sqrt{-(2\pi^2\rho_0r_0^2+1)^2} + i \right) \\
& - 8M^2n\omega \left( 2i\pi^2\rho_0r_0^2 + \sqrt{-(2\pi^2\rho_0r_0^2+1)^2} + i \right) (2\pi^2\rho_0r_0^2+1) \\
& + 2Mn^2 (2\pi^2\rho_0r_0^2+1)^3 - s^2 (2\pi^2\rho_0r_0^2+1)^4.
\end{aligned} \tag{25}$$

Defining the convergence series as  $S_n = a_n/a_{n-1}$ , then the recurrence relation can be expressed as

$$S_n = \frac{-\gamma_n}{\beta_n + \alpha_n S_{n+1}}. \tag{26}$$

Therefore, we obtain the main equation of the continued fraction method

$$0 = \beta_0 - \frac{\alpha_0\gamma_1}{\beta_1 - \frac{\alpha_1\gamma_2}{\beta_2 - \frac{\alpha_2\gamma_3}{\beta_3 - \dots}}}. \tag{27}$$

For specified values of the angular quantum number  $l$  and parameters, the determination of the quasinormal frequency  $\omega$  reduces to solving the main equation of the continued fraction method. In this formulation, the quasinormal frequency  $\omega$  is identified as the root of the continued fraction equation, which ensures both accuracy and numerical stability in the computation of quasinormal modes.

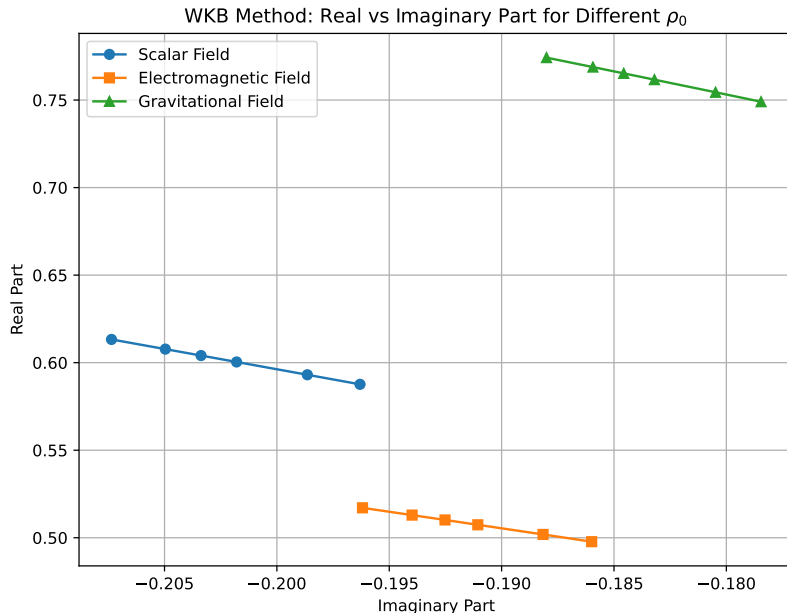


FIG. 1: The plot illustrates the relationship between the real and imaginary parts of the QNM frequencies using the WKB method for different values of  $\rho_0$  from Table I.

## B. Numerical methods for time-domain profiles

For the time-domain profile, we can calculate it using the numerical method suggested by Gundlach and Price et al. [29, 30]. When using the following light cone coordinates

$$\begin{aligned}
u &= t - r_*, \\
v &= t + r_*, 
\end{aligned} \tag{28}$$

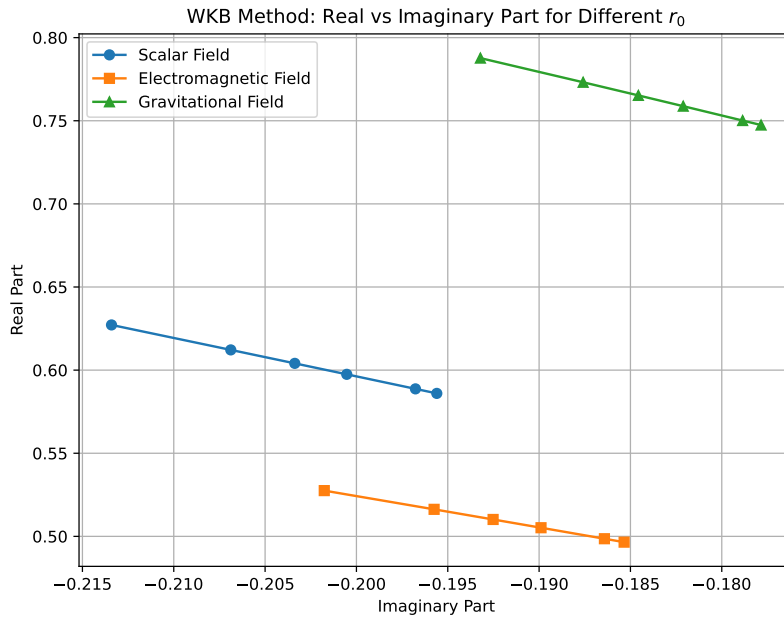


FIG. 2: The plot above illustrate the relationship between the real and imaginary parts of the QNM frequencies using the WKB method for  $r_0$  from Table I.

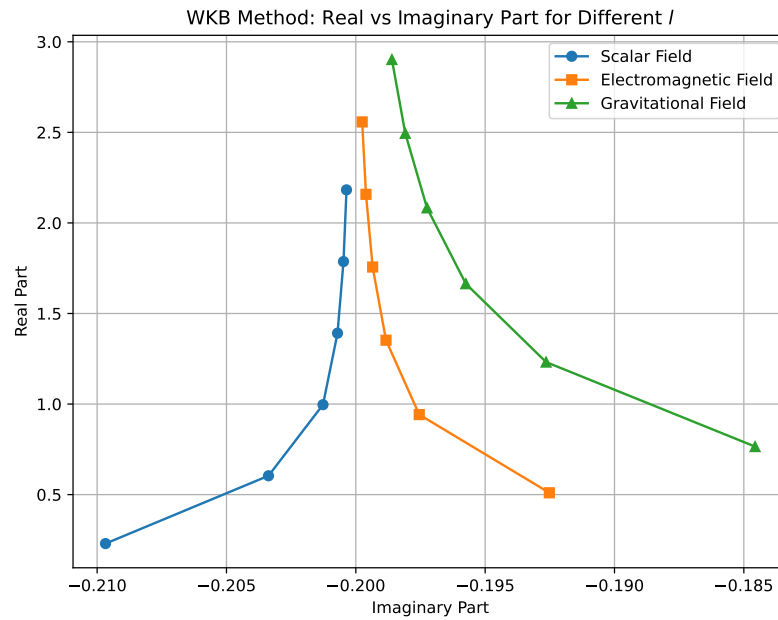


FIG. 3: The plot above illustrate the relationship between the real and imaginary parts of the QNM frequencies using the WKB method for  $l$  from Table I.

TABLE I: The QNM frequencies of scalar field perturbation.

$M = 0.5, l = 1, \rho_0 = 0.1$		
$r_0$	WKB method ( $2M\omega$ )	Continuous fraction method ( $2M\omega$ )
0.01	0.586001 - 0.195601 <i>i</i>	0.585988 - 0.195359 <i>i</i>
0.04	0.588724 - 0.196769 <i>i</i>	0.587723 - 0.195937 <i>i</i>
0.08	0.597473 - 0.20053 <i>i</i>	0.593274 - 0.197787 <i>i</i>
0.10	0.604067 - 0.203375 <i>i</i>	0.597437 - 0.199175 <i>i</i>
0.12	0.612165 - 0.206879 <i>i</i>	0.602525 - 0.200872 <i>i</i>
0.15	0.627181 - 0.213408 <i>i</i>	0.611893 - 0.203995 <i>i</i>
$M = 0.5, l = 1, r_0 = 0.1$		
$\rho_0$	WKB method ( $2M\omega$ )	Continuous fraction method ( $2M\omega$ )
0.01	0.587634 - 0.196301 <i>i</i>	0.587029 - 0.195706 <i>i</i>
0.04	0.593092 - 0.198645 <i>i</i>	0.590498 - 0.196862 <i>i</i>
0.08	0.60040 - 0.201792 <i>i</i>	0.595124 - 0.198404 <i>i</i>
0.10	0.604067 - 0.203375 <i>i</i>	0.597437 - 0.199175 <i>i</i>
0.12	0.607743 - 0.204964 <i>i</i>	0.59975 - 0.199947 <i>i</i>
0.15	0.613272 - 0.207359 <i>i</i>	0.603219 - 0.201103 <i>i</i>
$M = 0.5, r_0 = 0.1, \rho_0 = 0.1$		
$l$	WKB method ( $2M\omega$ )	Continuous fraction method ( $2M\omega$ )
0	0.229737 - 0.209676 <i>i</i>	0.22527 - 0.213933 <i>i</i>
1	0.604067 - 0.203375 <i>i</i>	0.597437 - 0.199175 <i>i</i>
2	0.996557 - 0.201269 <i>i</i>	0.986381 - 0.197337 <i>i</i>
3	1.39127 - 0.200707 <i>i</i>	1.37739 - 0.196809 <i>i</i>
4	1.78672 - 0.200476 <i>i</i>	1.76908 - 0.196589 <i>i</i>
5	2.182503 - 0.20036 <i>i</i>	2.16106 - 0.196477 <i>i</i>

the wave equations under different perturbations can always be expressed in the following form

$$\frac{\partial^2}{\partial u \partial v} \psi(u, v) + \frac{1}{4} V(r) \psi(u, v) = 0. \quad (29)$$

We will adopt the discretization scheme

$$\psi_N = \psi_E + \psi_W - \psi_S - \Delta u \Delta v V \left( \frac{\psi_W + \psi_E}{8} \right) + \mathcal{O}(\Delta^4). \quad (30)$$

TABLE II: The QNM frequencies of electromagnetic field perturbation.

$M = 0.5, l = 1, \rho_0 = 0.1$		
$r_0$	WKB method ( $2M\omega$ )	Continuous fraction method ( $2M\omega$ )
0.01	0.49652 - 0.185346 <i>i</i>	0.496606 - 0.18501 <i>i</i>
0.04	0.498583 - 0.186424 <i>i</i>	0.497795 - 0.18552 <i>i</i>
0.08	0.505197 - 0.189895 <i>i</i>	0.501589 - 0.187153 <i>i</i>
0.10	0.510171 - 0.192518 <i>i</i>	0.504423 - 0.188376 <i>i</i>
0.12	0.516265 - 0.195748 <i>i</i>	0.507873 - 0.189869 <i>i</i>
0.15	0.527526 - 0.201761 <i>i</i>	0.514183 - 0.192611 <i>i</i>
$M = 0.5, l = 1, r_0 = 0.1$		
$\rho_0$	WKB method ( $2M\omega$ )	Continuous fraction method ( $2M\omega$ )
0.01	0.497758 - 0.185992 <i>i</i>	0.49732 - 0.185316 <i>i</i>
0.04	0.501888 - 0.188156 <i>i</i>	0.499694 - 0.186337 <i>i</i>
0.08	0.507406 - 0.191059 <i>i</i>	0.50285 - 0.187697 <i>i</i>
0.10	0.510171 - 0.192518 <i>i</i>	0.504423 - 0.188376 <i>i</i>
0.12	0.512939 - 0.193983 <i>i</i>	0.505993 - 0.189055 <i>i</i>
0.15	0.517097 - 0.19619 <i>i</i>	0.508342 - 0.190072 <i>i</i>
$M = 0.5, r_0 = 0.1, \rho_0 = 0.1$		
$l$	WKB method ( $2M\omega$ )	Continuous fraction method ( $2M\omega$ )
1	0.510171 - 0.192518 <i>i</i>	0.504423 - 0.188376 <i>i</i>
2	0.941856 - 0.197548 <i>i</i>	0.932187 - 0.193685 <i>i</i>
3	1.35249 - 0.198833 <i>i</i>	1.33898 - 0.194971 <i>i</i>
4	1.75665 - 0.199349 <i>i</i>	1.73929 - 0.195482 <i>i</i>
5	2.15793 - 0.199607 <i>i</i>	2.13672 - 0.195738 <i>i</i>
6	2.55769 - 0.199754 <i>i</i>	2.53262 - 0.195884 <i>i</i>

where  $S = (u, v)$ ,  $W = (u + \Delta u, v)$ ,  $E = (u, v + \Delta v)$ ,  $N = (u + \Delta u, v + \Delta v)$ . Moreover, we use the Gaussian initial pulse [31]

$$\begin{aligned} \psi(u = u_0, v) &= \exp \left[ -\frac{(v - v_c)^2}{2\sigma^2} \right], \\ \psi(u, v = v_0) &= 0. \end{aligned} \quad (31)$$

in this work, we take  $\sigma = 3$ ,  $v_c = 10$ . Therefore, we can always calculate the next grid point  $\psi_N$  based on the known three grid points. By repeating this process, all the points on the entire grid can be calculated. Using this method, we have plotted the time-domain evolution results of BH surrounded by the Burkert profile DM halo, as shown in Fig. 4 - Fig.6.

TABLE III: The QNM frequencies of gravitational perturbation.

$M = 0.5, l = 2, \rho_0 = 0.1$		
$r_0$	WKB method ( $2M\omega$ )	Continuous fraction method ( $2M\omega$ )
0.01	0.747419 - 0.177849 <i>i</i>	0.747445 - 0.177957 <i>i</i>
0.04	0.750122 - 0.178859 <i>i</i>	0.748962 - 0.17844 <i>i</i>
0.08	0.758767 - 0.18211 <i>i</i>	0.75379 - 0.179983 <i>i</i>
0.10	0.765243 - 0.184566 <i>i</i>	0.757382 - 0.18114 <i>i</i>
0.12	0.77315 - 0.187589 <i>i</i>	0.761739 - 0.182554 <i>i</i>
0.15	0.78768 - 0.193214 <i>i</i>	0.769663 - 0.185154 <i>i</i>
$M = 0.5, l = 2, r_0 = 0.1$		
$\rho_0$	WKB method ( $2M\omega$ )	Continuous fraction method ( $2M\omega$ )
0.01	0.749041 - 0.178455 <i>i</i>	0.748356 - 0.178246 <i>i</i>
0.04	0.754446 - 0.180481 <i>i</i>	0.751382 - 0.179212 <i>i</i>
0.08	0.761646 - 0.1832 <i>i</i>	0.755389 - 0.180498 <i>i</i>
0.10	0.765243 - 0.184566 <i>i</i>	0.757382 - 0.18114 <i>i</i>
0.12	0.768838 - 0.185937 <i>i</i>	0.759367 - 0.181783 <i>i</i>
0.15	0.774228 - 0.188003 <i>i</i>	0.76233 - 0.182747 <i>i</i>
$M = 0.5, r_0 = 0.1, \rho_0 = 0.1$		
$l$	WKB method ( $2M\omega$ )	Continuous fraction method ( $2M\omega$ )
2	0.765243 - 0.184566 <i>i</i>	0.757382 - 0.18114 <i>i</i>
3	1.23175 - 0.192644 <i>i</i>	1.21939 - 0.188903 <i>i</i>
4	1.66438 - 0.195748 <i>i</i>	1.64791 - 0.191951 <i>i</i>
5	2.08311 - 0.197248 <i>i</i>	2.06262 - 0.193425 <i>i</i>
6	2.4947 - 0.198088 <i>i</i>	2.47025 - 0.19425 <i>i</i>
7	2.90212 - 0.198605 <i>i</i>	2.87373 - 0.194758 <i>i</i>

## V. DISCUSSION OF QUASINORMAL MODES FOR A BH SURROUNDED BY A BURKETT PROFILE DM HALO

The computed quasinormal mode (QNM) frequencies for scalar, electromagnetic, and gravitational perturbations around a BH surrounded by a Burkett profile DM halo exhibit intriguing patterns as shown in Fig.1, Fig.2 and Fig3. The QNMs are calculated using the WKB and continuous fraction methods, with variations in the parameters  $r_0$ ,  $\rho_0$ , and  $l$  as shown in Table I, Table II and Table III. For scalar field perturbations, the real part of the QNM frequency,  $\text{Re}(\omega)$ , increases with  $r_0$ , indicating that the oscillation frequency grows as the distance  $r_0$  from the BH increases. The imaginary part,  $\text{Im}(\omega)$ , also increases in magnitude, reflecting stronger damping for larger  $r_0$ . Similarly, higher values of  $\rho_0$  slightly enhance both the oscillation frequency and the damping rate, suggesting that the DM density influences the perturbations. As the multipole number  $l$  increases, the real part grows significantly, while the imaginary part shows a relatively modest increase, indicating faster but less strongly damped oscillations.

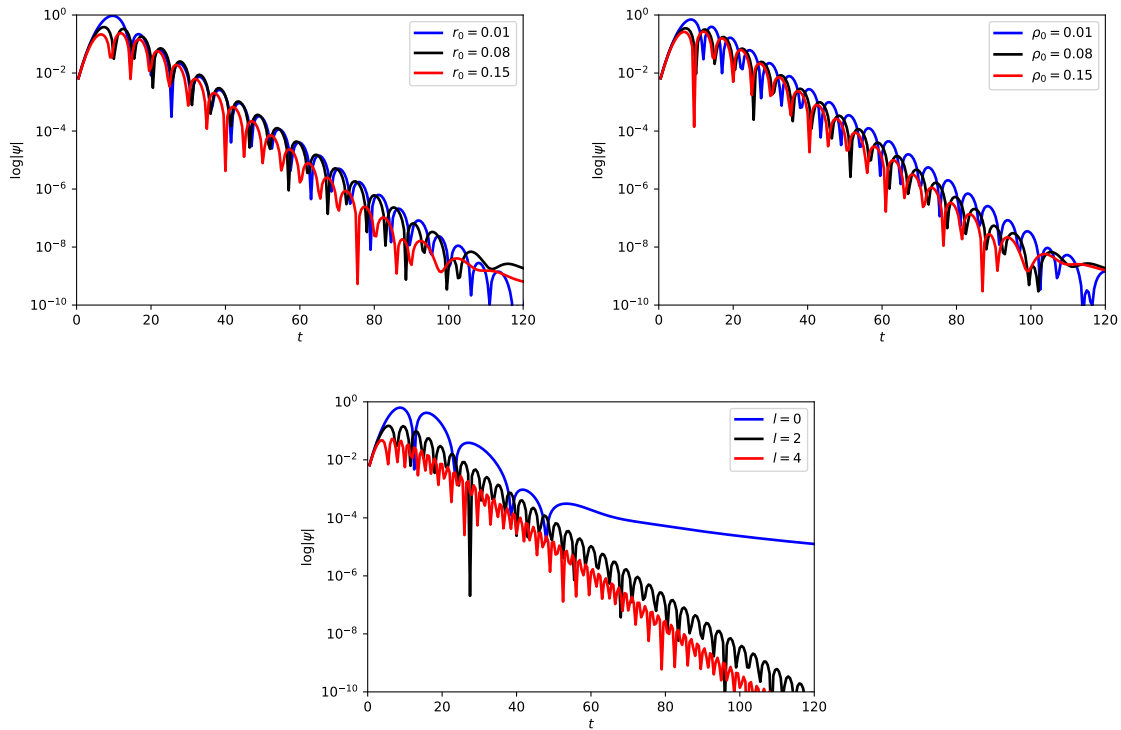


FIG. 4: The time-domain profiles of the scalar field perturbation for different  $r_0$  with  $M = 0.5$ ,  $l = 1$ ,  $\rho_0 = 0.1$ , for different  $\rho_0$  with  $M = 0.5$ ,  $l = 1$ ,  $r_0 = 0.1$ , and for different  $l$  with  $M = 0.5$ ,  $r_0 = 0.1$ ,  $\rho_0 = 0.1$ , respectively.

For electromagnetic field perturbations, similar trends are observed. The QNMs exhibit an increase in both  $\text{Re}(\omega)$  and  $\text{Im}(\omega)$  with growing  $r_0$ ,  $\rho_0$ , and  $l$ , showing that the Burkett profile DM halo subtly impacts the oscillatory and damping properties of these perturbations. Notably, the differences between the WKB and continuous fraction methods are minimal, with the WKB method generally yielding slightly higher real and imaginary parts.

Gravitational perturbations also demonstrate a consistent increase in  $\text{Re}(\omega)$  and  $\text{Im}(\omega)$  with  $r_0$  and  $\rho_0$ , while higher multipole moments correspond to faster oscillations and slightly stronger damping. The results reveal a systematic sensitivity of the QNMs to the parameters of the Burkett halo, suggesting that DM density and distance influence the effective potential governing the perturbations. The agreement between the WKB and continuous fraction methods, despite minor deviations, underscores the reliability of these results. These findings provide a foundation for probing the effects of DM halos on BHs through gravitational wave observations, offering a potential avenue to test the interplay between BHs and their surrounding DM environments.

## VI. CONCLUSION

We have presented an analytic construction of a Schwarzschild-like BH surrounded by a Burkert DM halo and analyzed its linear response to scalar, electromagnetic, and gravitational perturbations. The metric is obtained by matching the halo-only solution-derived from the rotation-curve relation-to the full Einstein system with a vacuum BH core, yielding  $F_1(r) = F_2(r) = \mathcal{N}_{Bur}(r) - 2M/r$  with  $\mathcal{N}_{Bur}(r)$  fixed by the halo parameters  $(\rho_0, r_0)$ . On this background we computed quasinormal modes via both WKB and continued-fraction techniques and verified the ringdown behavior through time-domain profiles. Across all spins we observe consistent trends: larger  $(\rho_0, r_0)$  strengthen the effective potential, increasing  $\text{Re}(\omega)$  and the magnitude of  $\text{Im}(\omega)$ , while higher  $l$  primarily raises the oscillation frequency with comparatively modest damping changes. The close agreement between the two frequency-extraction methods indicates numerical robustness, and the spectrum continuously recovers the Schwarzschild limit as the halo contribution is diluted. These results provide a controlled setting to quantify environmental effects on BH ringdowns in cored halos and can be used to inform parameterized tests with current and future gravitational-wave data. Natural extensions include incorporating rotation, comparing different halo models (e.g., NFW/Einasto vs. Burkert), adding massive or self-interacting fields, and exploring lensing/shadow observables in the same geometry to build

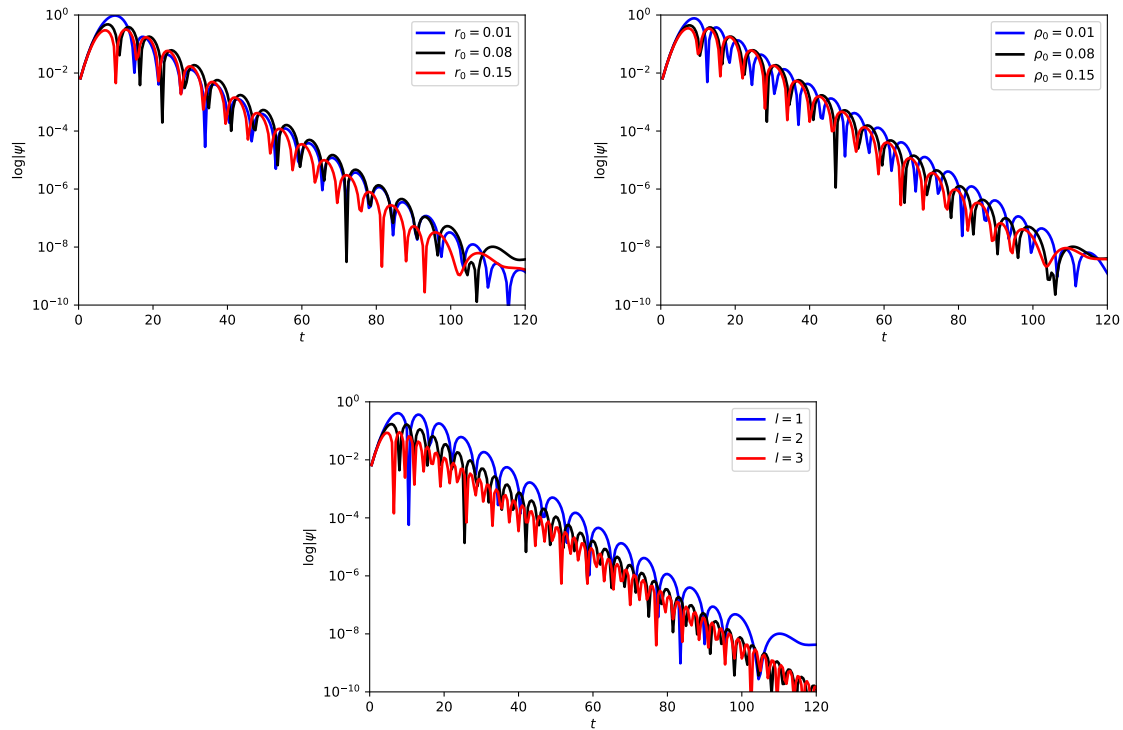


FIG. 5: The time-domain profiles of the electromagnetic field perturbation for different  $r_0$  with  $M = 0.5, l = 1, \rho_0 = 0.1$ , for different  $\rho_0$  with  $M = 0.5, l = 1, r_0 = 0.1$ , and for different  $l$  with  $M = 0.5, r_0 = 0.1, \rho_0 = 0.1$ , respectively.

a multi-messenger probe of DM distributions around BHs.

### Acknowledgments

This research was funded by the National Natural Science Foundation of China (No. 12505064), Guizhou Provincial Basic Research Program (Natural Science) Youth Guidance Program (No. QN [2025] 365) and the project of Young Scientific and Technical Talents Development of Education Department of Guizhou Province under Grant [2024] 79. G. L and A. Ö. would like to acknowledge networking support of the COST Action CA21106 - COSMIC WISPer in the Dark Universe: Theory, astrophysics and experiments (CosmicWISPer), the COST Action CA22113 - Fundamental challenges in theoretical physics (THEORY-CHALLENGES), the COST Action CA21136 - Addressing observational tensions in cosmology with systematics and fundamental physics (CosmoVerse), the COST Action CA23130 - Bridging high and low energies in search of quantum gravity (BridgeQG), and the COST Action CA23115 - Relativistic Quantum Information (RQI) funded by COST (European Cooperation in Science and Technology). A. Ö. also thanks to EMU, TUBITAK, ULAKBIM (Turkiye) and SCOAP3 (Switzerland) for their support.

---

[1] PLANCK collaboration, *Planck 2018 results. VI. Cosmological parameters*, *Astron. Astrophys.* **641** (2020) A6 [[1807.06209](#)].  
[2] W.J.G. de Blok, *The Core-Cusp Problem*, *Adv. Astron.* **2010** (2010) 789293 [[0910.3538](#)].  
[3] F. Donato, G. Gentile, P. Salucci, C.F. Martins, M.I. Wilkinson, G. Gilmore et al., *A constant dark matter halo surface density in galaxies*, *Mon. Not. Roy. Astron. Soc.* **397** (2009) 1169 [[0904.4054](#)].  
[4] G. Seo, J. Sohn and M.G. Lee, *Tracing Dark Matter Halos with Satellite Kinematics and the Central Stellar Velocity Dispersion of Galaxies*, *Astrophys. J.* **903** (2020) 130 [[2010.00693](#)].  
[5] J.F. Navarro, C.S. Frenk and S.D.M. White, *The Structure of cold dark matter halos*, *Astrophys. J.* **462** (1996) 563 [[astro-ph/9508025](#)].

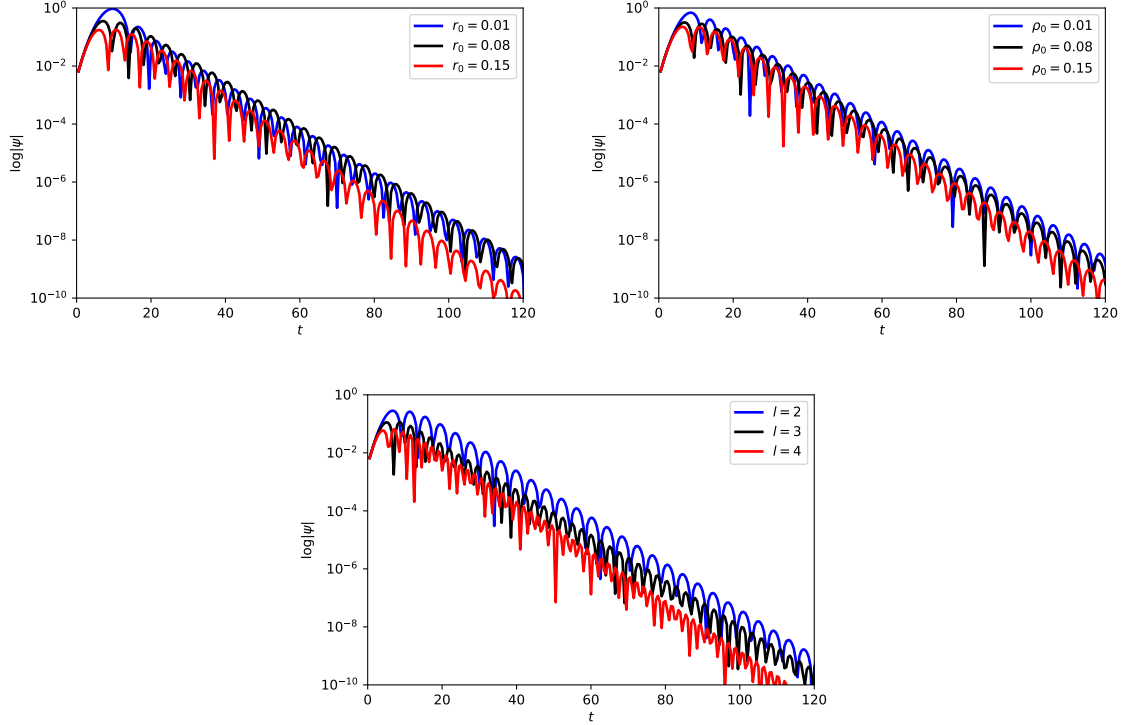


FIG. 6: The time-domain profiles of the gravitational perturbation for different  $r_0$  with  $M = 0.5$ ,  $l = 2$ ,  $\rho_0 = 0.1$ , for different  $\rho_0$  with  $M = 0.5$ ,  $l = 2$ ,  $r_0 = 0.1$ , and for different  $l$  with  $M = 0.5$ ,  $r_0 = 0.1$ ,  $\rho_0 = 0.1$ , respectively.

- [6] A. Burkert, *The Structure of dark matter halos in dwarf galaxies*, *Astrophys. J. Lett.* **447** (1995) L25 [[astro-ph/9504041](#)].
- [7] P. Salucci and A. Burkert, *Dark matter scaling relations*, *Astrophys. J. Lett.* **537** (2000) L9 [[astro-ph/0004397](#)].
- [8] K.-i. Maeda, V. Cardoso and A. Wang, *Einstein cluster as central spiky distribution of galactic dark matter*, *Phys. Rev. D* **111** (2025) 044060 [[2410.04175](#)].
- [9] P.G.S. Fernandes and V. Cardoso, *Dark matter as a vector field: an action principle for the Einstein cluster*, [2505.00563](#).
- [10] E. Figueiredo, A. Maselli and V. Cardoso, *Black holes surrounded by generic dark matter profiles: Appearance and gravitational-wave emission*, *Phys. Rev. D* **107** (2023) 104033 [[2303.08183](#)].
- [11] A. Övgün and R.C. Pantig, *Black hole in the Dekel-Zhao dark matter profile*, *Phys. Lett. B* **864** (2025) 139398 [[2501.12559](#)].
- [12] A. Övgün, L.J.F. Sese and R.C. Pantig, *Constraints via the Event Horizon Telescope for Black Hole Solutions with Dark Matter under the Generalized Uncertainty Principle Minimal Length Scale Effect*, *Annalen Phys.* **536** (2024) 2300390 [[2309.07442](#)].
- [13] Y. Yang, D. Liu, A. Övgün, G. Lambiase and Z.-W. Long, *Black hole surrounded by the pseudo-isothermal dark matter halo*, *Eur. Phys. J. C* **84** (2024) 63 [[2308.05544](#)].
- [14] R.C. Pantig and A. Övgün, *Black Hole in Quantum Wave Dark Matter*, *Fortsch. Phys.* **71** (2023) 2200164 [[2210.00523](#)].
- [15] D. Liu, Y. Yang, A. Övgün, Z.-W. Long and Z. Xu, *Gravitational ringing and superradiant instabilities of the Kerr-like black holes in a dark matter halo*, *Eur. Phys. J. C* **83** (2023) 565 [[2204.11563](#)].
- [16] R.C. Pantig and A. Övgün, *Dark matter effect on the weak deflection angle by black holes at the center of Milky Way and M87 galaxies*, *Eur. Phys. J. C* **82** (2022) 391 [[2201.03365](#)].
- [17] S. Islam, F. Rahaman, A. Övgün and M. Halilsoy, *Formation of Wormholes by Dark Matter in the Galaxy Dragonfly 44*, *Can. J. Phys.* **97** (2019) 241 [[1806.01135](#)].
- [18] A. Burkert, *The Structure of dark matter halos in dwarf galaxies*, *Astrophys. J. Lett.* **447** (1995) L25 [[astro-ph/9504041](#)].
- [19] T. Matos, F.S. Guzman and D. Nunez, *Spherical scalar field halo in galaxies*, *Phys. Rev. D* **62** (2000) 061301 [[astro-ph/0003398](#)].
- [20] Z. Xu, X. Hou, X. Gong and J. Wang, *Black Hole Space-time In Dark Matter Halo*, *JCAP* **09** (2018) 038 [[1803.00767](#)].
- [21] E. Berti, V. Cardoso and A.O. Starinets, *Quasinormal modes of black holes and black branes*, *Class. Quant. Grav.* **26** (2009) 163001 [[0905.2975](#)].
- [22] R.A. Konoplya and A. Zhidenko, *Quasinormal modes of black holes: From astrophysics to string theory*, *Rev. Mod. Phys.* **83** (2011) 793 [[1102.4014](#)].
- [23] V. Cardoso and P. Pani, *Testing the nature of dark compact objects: a status report*, *Living Rev. Rel.* **22** (2019) 4 [[1904.05363](#)].
- [24] LIGO SCIENTIFIC, VIRGO collaboration, *Observation of Gravitational Waves from a Binary Black Hole Merger*, *Phys. Rev. Lett.* **116** (2016) 061102 [[1602.03837](#)].

- [25] T. Matos and D. Nunez, *The general relativistic geometry of the Navarro - Frenk - White model*, *Rev. Mex. Fis.* **51** (2005) 71 [[astro-ph/0303594](#)].
- [26] Z. Xu, X. Hou, X. Gong and J. Wang, *Black Hole Space-time In Dark Matter Halo*, *JCAP* **09** (2018) 038 [[1803.00767](#)].
- [27] E.W. Leaver, *An Analytic representation for the quasi normal modes of Kerr black holes*, *Proc. Roy. Soc. Lond. A* **402** (1985) 285.
- [28] E.W. Leaver, *Quasinormal modes of Reissner-Nordstrom black holes*, *Phys. Rev. D* **41** (1990) 2986.
- [29] C. Gundlach, R.H. Price and J. Pullin, *Late time behavior of stellar collapse and explosions: 1. Linearized perturbations*, *Phys. Rev. D* **49** (1994) 883 [[gr-qc/9307009](#)].
- [30] C. Gundlach, R.H. Price and J. Pullin, *Late time behavior of stellar collapse and explosions: 2. Nonlinear evolution*, *Phys. Rev. D* **49** (1994) 890 [[gr-qc/9307010](#)].
- [31] R. Moderski and M. Rogatko, *Late time evolution of a charged massless scalar field in the space-time of a dilaton black hole*, *Phys. Rev. D* **63** (2001) 084014.